Steady states and oscillatory instability of swirling flow in a cylinder with rotating top and bottom

Alexander Yu. Gelfgat, Pinhas Z. Bar-Yoseph,[a] and Alexander Solan
Computational Mechanics Laboratory, Faculty of Mechanical Engineering, Technion-Israel Institute of Technology, Haifa 32000, Israel

(Received 15 February 1996; accepted 7 June 1996)

In this study we present a numerical investigation of steady states, onset of oscillatory instability, and slightly supercritical oscillatory states of an axisymmetric swirling flow of a Newtonian incompressible fluid in a cylinder, with independently rotating top and bottom. The first part of the study is devoted to the influence of co- and counter-rotation of the bottom on the steady vortex breakdown, which takes place in the well-known problem of flow in a cylinder with a rotating top. It is shown that weak counter-rotation of the bottom may suppress the vortex breakdown. Stronger counter-rotation may induce a stable steady vortex breakdown at relatively large Reynolds numbers for which a vortex breakdown does not appear in the case of the stationary bottom. Weak corotation may promote the vortex breakdown at lower Reynolds numbers than in the cylinder with the stationary bottom. Stronger corotation leads to the detachment of the recirculation zone from the axis and the formation of an additional vortex ring. The second part of the study is devoted to the investigation of the onset of oscillatory instability of steady flows. It is shown that the oscillatory instability sets in due to a Hopf bifurcation. The critical Reynolds number and the critical frequency of oscillations were calculated as a function of the rotation ratio ($\xi = \Omega_{\text{bottom}}/\Omega_{\text{top}}$) for a fixed value of the aspect ratio γ (height/radius) of the cylinder $\gamma = 1.5$. The stability analysis showed that there are several most unstable linear modes of the perturbation that become successively dominant with a continuous change of ξ. It is shown that the oscillatory instability may lead to an appearance and coexistence of more than one oscillating separation vortex bubble. © *1996 American Institute of Physics.* [S1070-6631(96)00110-9]

I. INTRODUCTION

Vortex breakdown in a cylinder with a rotating top was discovered experimentally by Vogel[1] and has been intensively studied experimentally[2–5] and numerically.[6–12] The vortex breakdown observed in this system is characterized by the sudden appearance of a weak meridional recirculation (also called ''separation vortex bubble'') near the axis of the cylinder. It was shown by Gelfgat *et al.*[11] that the appearance of the vortex breakdown in this flow is not caused by instability, and that with the increase of the Reynolds number the separation vortex bubble appears and disappears along a continuous branch of the steady solution.

The influence of weak co- and counter-rotation of the bottom of the cylinder on the vortex breakdown was studied experimentally by Roesner[3] and Bar-Yoseph *et al.*[4] It was shown that weak corotation of the bottom may promote a separation vortex bubble in a flow without meridional recirculation. Conversely, weak counter-rotation of the bottom may suppress an existing separation vortex bubble and change the meridional flow to a single-vortex state. A similar effect of the co- and counter-rotation on the vortex breakdown was observed by Bar-Yoseph *et al.*,[13] Bar-Yoseph,[14,15] and Bar-Yoseph and Kryzhanovski[16,17] in the polar region between rotating spheres.

A numerical study by Valentine and Jahnke[18] was devoted to a particular symmetric case when the top and the bottom corotate with the same angular velocity. It was shown[18] that such corotation leads to the detachment of the recirculation zone from the axis and the formation of up to four vortex rings, two above and two below the plane of symmetry. This result is in agreement with the experiments of Spohn *et al.*,[19] who investigated the flow in a cylinder with rotating bottom and a stress–free surface at the top. To compare both results one should associate the stress–free boundary of the experimental setup[19] with the horizontal plane of symmetry of the mathematical model.[18] Lopez[20] investigated the transition from the steady to the oscillatory state for $\gamma = 3$ in the case when the top and the bottom corotate with the same angular velocity ($\xi = 1$). Parametric investigation of the oscillatory instability in this case for the interval $1 \leqslant \gamma \leqslant 3$ was done recently by Gelfgat *et al.*[21]

The independent rotation of the bottom is characterized by the ratio of angular velocities $\xi = \Omega_{\text{bottom}}/\Omega_{\text{top}}$ (rotation ratio). If $|\Omega_{\text{top}}| \geqslant |\Omega_{\text{bottom}}|$, ξ varies in the interval $-1 \leqslant \xi \leqslant 1$. Otherwise, the cylinder may be turned over such that top and bottom replace each other, implying that Re and ξ are replaced by $\xi\,\text{Re}$ and $1/\xi$. The experiments of Roesner[3,4] were done for $|\xi| \leqslant 0.1$. The numerical analysis of Valentine and Jahnke,[18] Lopez,[20] and Gelfgat *et al.*[21] was carried out mainly for $\xi = 1$. Flows corresponding to other values of ξ were not studied.

The stability of steady flows in the cylinder with rotating top and stationary bottom ($\xi = 0$) was studied by Gelfgat *et al.*[11] for aspect ratio $1 \leqslant \gamma \leqslant 3.5$. It was shown that the appearance and disappearance of the vortex breakdown is not connected with the stability of the flow. It was also shown

[a]Corresponding author. Fax: 972-4-8324533;
electronic mail: merbygr@cmlp.technion.ac.il

 1070-6631/96/8(10)/2614/12/$10.00

that for $\gamma \leqslant 3$ the oscillatory instability sets in as a result of an axisymmetric supercritical Hopf bifurcation, and that the oscillatory instability may promote the oscillatory vortex breakdown in cases for which the *steady* vortex breakdown is not found.

The present study is devoted to the analysis of the effect of co- and counter-rotation on steady flows and on the onset of oscillatory instability. The analysis is carried out for the whole interval $-1 \leqslant \xi \leqslant 1$.

An investigation of the suppression of the vortex breakdown by the counter-rotation of the bottom shows that the higher the cylinder (the larger the aspect ratio) the weaker the counter-rotation necessary to eliminate a recirculation zone from the flow. It is also shown that the counter-rotation may stabilize the steady flow and induce a stable steady vortex breakdown at relatively large Reynolds numbers, for which in the case of stationary bottom there exists an unstable steady state without a vortex breakdown.

In the case of corotation it is shown that the separation vortex bubble, characteristic for $\xi=0$, and the vortex ring, characteristic for $\xi=1$, continuously transform one into the other when ξ is continuously varied between 0 and 1. It is also shown that weak corotation induces the vortex breakdown at lower Reynolds numbers than for $\xi=0$.

The stability of steady states was studied for a fixed value of the aspect ratio $\gamma=1.5$. The steady flows considered remain stable up to the onset of the oscillatory instability, which takes place due to the Hopf bifurcation. The instability may set in with the increase of the Reynolds number Re or with the change of the rotation ratio ξ. The main results of the stability analysis are presented in stability diagrams plotted in the plane (ξ,Re). The dependence of the critical frequency of oscillations on the rotation ratio is also reported. It is shown that the oscillatory instability may be caused by different most unstable linear modes that become dominant for different parameter values. Examples of patterns of the most unstable linear modes are reported, together with the patterns of the flow at critical values of parameters. Possible reasons that may cause the onset of the instability are discussed.

Slightly supercritical states of the flow were calculated using the finite volume method for the solution of the full unsteady Navier–Stokes equations. A numerical solution of the full unsteady problem was used to verify results of the linear stability analysis and to investigate the oscillatory states of the flow.

II. FORMULATION OF THE PROBLEM AND NUMERICAL TECHNIQUE

The axisymmetric flow of an incompressible Newtonian fluid with kinematic viscosity ν^* in a cylinder of radius R^* and height H^*, with top and bottom rotating with angular velocities Ω^*_{top} and $\Omega^*_{\mathrm{bottom}}$ is considered. The flow is described by the momentum and continuity equations in a cylindrical system of coordinates (r,φ,z). Using the scales R^*, R^{*2}/ν^*, $\Omega^*_{\mathrm{top}}R^*$, and $\rho^*(\Omega^*_{\mathrm{top}}R^*)^2$ for length, time, velocity, and pressure, respectively, the dimensionless equations are

$$\begin{gathered}\frac{\partial v_r}{\partial t}+v_r\frac{\partial v_r}{\partial r}+v_z\frac{\partial v_r}{\partial z}-\frac{v_\varphi^2}{r}\\ =-\frac{\partial p}{\partial r}+\frac{1}{\mathrm{Re}}\left(\frac{\partial^2 v_r}{\partial r^2}+\frac{1}{r}\frac{\partial v_r}{\partial r}+\frac{\partial^2 v_r}{\partial z^2}-\frac{v_r}{r^2}\right),\\ \frac{\partial v_\varphi}{\partial t}+v_r\frac{\partial v_\varphi}{\partial r}+v_z\frac{\partial v_\varphi}{\partial z}+\frac{v_r v_\varphi}{r}\\ =\frac{1}{\mathrm{Re}}\left(\frac{\partial^2 v_\varphi}{\partial r^2}+\frac{1}{r}\frac{\partial v_\varphi}{\partial r}+\frac{\partial^2 v_\varphi}{\partial z^2}-\frac{v_\varphi}{r^2}\right),\end{gathered}\tag{1}$$

$$\begin{gathered}\frac{\partial v_z}{\partial t}+v_r\frac{\partial v_z}{\partial r}+v_z\frac{\partial v_z}{\partial z}\\ =-\frac{\partial p}{\partial z}+\frac{1}{\mathrm{Re}}\left(\frac{\partial^2 v_z}{\partial r^2}+\frac{1}{r}\frac{\partial v_z}{\partial r}+\frac{\partial^2 v_z}{\partial z^2}\right),\\ \frac{\partial v_r}{\partial r}+\frac{v_r}{r}+\frac{\partial v_z}{\partial z}=0.\end{gathered}\tag{2}$$

At the axis of the cylinder $(0\leqslant z\leqslant\gamma,\ r=0)$ the boundary conditions of an axisymmetric flow are

$$v_r=v_\varphi=\frac{\partial v_z}{\partial r}=0,\tag{3}$$

on the cylindrical wall $(0\leqslant z<\gamma,\ r=1)$,

$$v_r=v_\varphi=v_z=0,\tag{4}$$

on the rotating top of the cylinder $(0\leqslant r<1,\ z=\gamma)$,

$$v_r=v_z=0,\quad v_\varphi=r,\tag{5}$$

and on the rotating bottom of the cylinder $(0\leqslant r<1,\ z=0)$,

$$v_r=v_z=0,\quad v_\varphi=\xi r.\tag{6}$$

Here $\mathrm{Re}=\Omega^*_{\mathrm{top}}R^{*2}/\nu^*$ is the Reynolds number, $\xi=\Omega^*_{\mathrm{bottom}}/\Omega^*_{\mathrm{top}}$ is the rotation ratio, and $\gamma=H^*/R^*$ is the aspect ratio of the cylinder. [Note that some authors define $\gamma=H^*/(2R^*)$.]

The problem (1)–(6) was solved numerically using the Galerkin spectral method for the calculation of steady states and linear stability analysis, and using the finite volume method for the calculation of steady and oscillatory states. The Galerkin method is formulated for globally defined basis functions that satisfy all the boundary conditions and the continuity equation. The basis functions are constructed as linear superpositions of Chebyshev polynomials with the help of symbolic computations. The finite volume method is of the second order in space and time. It is based on the SIMPLE algorithm[22] and three-levels approximation of the time derivative.[23] The finite volume grids are stretched such that the nodes are condensed near the axis, the top, the bottom, and the sidewall of the cylinder. A detailed description of the numerical algorithms and test calculations is reported in Refs. 11 and 12.

The spectral Galerkin method allows a sufficient decrease of the number of degrees of freedom used by a numerical method, which makes it possible to calculate steady states and to analyze their stability within the framework of the same numerical model. To analyze the linear stability of steady states the governing equations were linearized in the vicinity of a steady solution and the spectrum of the linearized problem was calculated and analyzed. The instability of the flow was indicated by the change of sign of the real part of the dominant eigenvalue Λ (the eigenvalue with the largest real part). The change of the sign takes place with the increase of the Reynolds number or with the change of the rotation ratio. The critical values of the Reynolds number $\mathrm{Re}_{\mathrm{cr}}$ and of the rotation ratio ξ_{cr}, for which $\mathrm{Real}(\Lambda)=0$, were calculated. In all the cases considered it was found that at the critical values of parameters $\mathrm{Im}(\Lambda)\neq 0$ and $(\partial/\partial\,\mathrm{Re})[\mathrm{Real}(\Lambda)]\neq 0$, which indicates that the instability sets in due to Hopf bifurcation (see Refs. 24 and 25 for details). This means that the circular frequency of the flow oscillations in the vicinity of $\mathrm{Re}=\mathrm{Re}_{\mathrm{cr}}$ may be estimated as $\omega_{\mathrm{cr}}=\mathrm{Im}(\Lambda)$. The eigenvector corresponding to the dominant eigenvalue $\Lambda=i\omega_{\mathrm{cr}}$ describes the most dominant perturbation, which causes the onset of instability. Since the eigenvector is a complex function and is defined within multiplication by a complex constant, its modulus is used to describe the dominant perturbations. Note that for slightly supercritical oscillatory flows the isolines of the amplitude of oscillations coincide with the isolines of the modulus of the perturbation. The dominant perturbation of the considered flow is described by the perturbations of the meridional streamfunction ψ $[v_r=(1/r)(\partial\psi/\partial z),\ v_z=-(1/r)(\partial\psi/\partial r)]$ and of the azimuthal moment $\mathscr{M}_\varphi=rv_\varphi$. In the following text these perturbations are called perturbation of the meridional component of the flow and perturbation of the azimuthal component of the flow, respectively.

The numerical technique was completely verified in Refs. 11 and 12 for the case $\xi=0$, for which a large amount of experimental and numerical data is available for comparison.[2–10] In the case $\xi\neq 0$ only the experimental results of Roesner[3] and the numerical results of Valentine and Jahnke[18] and Lopez[20] may be used for qualitative comparison with the results obtained here. The results obtained for $\xi\neq 0$ were validated in three ways: (1) it was ensured that further increase of the number of the Galerkin modes does not lead to significant quantitative changes in steady flows or critical parameters; (2) the steady solutions obtained with the Galerkin method were compared with those obtained by the finite volume method using stretched grids up to 100×100 nodes; and (3) the numerical solution of the full unsteady problem allowed us to localize the critical Reynolds numbers and to estimate critical frequencies, and then the critical parameters obtained by the two independent numerical approaches were compared. The steady states discussed in Sec. III A were calculated using 30×30 basis functions for the Galerkin method and a 75×75 stretched grid for the finite volume method. The stretching was the same as in Gelfgat *et al.*[11] The stability analysis was done with the number of basis functions varying from 30×30 to 40×40. The number of nodes for the unsteady calculations varied from 75×75 to 200×200. The details of the test calculations and of the dependence of the critical parameters on the discretization are discussed in the Appendix.

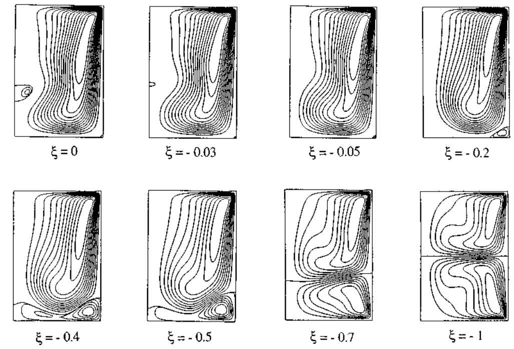

FIG. 1. Counter-rotating bottom. Streamlines. Here $\mathrm{Re}=1500$, $\gamma=1.5$, $0\geqslant\xi\geqslant-1$.

III. MAIN RESULTS

A. Steady states

1. Counter-rotating bottom

The change of the meridional flow with the continuous increase of the counter-rotation (decrease of ξ from $\xi=0$ to $\xi=-1$) is shown in Fig. 1 for the case $\gamma=1.5$, $\mathrm{Re}=1500$. One can see that weak counter-rotation eliminates the separation vortex bubble that exists at $\xi=0$. The separation bubble disappears when the angular velocity of the counter-rotating bottom exceeds 3% of the angular velocity of the top ($\xi=-0.03,-0.05$). This is in qualitative agreement with the experimental results of Roesner.[3,4] A further increase of the counter-rotation (decrease of ξ) up to $\xi=-0.2$ leads to the appearance of a meridional vortex in the lower corner of the cylinder ($\xi=-0.2$). Another recirculation region attached to the bottom appears with an additional decrease of ξ ($\xi=-0.4$). When the rotation ratio reaches the value $\xi=-0.5$ the two regions attached to the bottom join and form one counterclockwise recirculation region ($\xi=-0.5$). This region grows with the increase of the counter-rotation, while the upper clockwise recirculation region becomes smaller (ξ varying from -0.7 to -1). Both clockwise and counterclockwise recirculation regions become antisymmetric when ξ reaches the value $\xi=-1$.

Figures 2 and 3 illustrate the suppression of the vortex breakdown by counter-rotation in cylinders with aspect ratio $\gamma=2$ and 2.5 and for the same value of the Reynolds number $\mathrm{Re}=2000$. In the case of rotating top and stationary bottom ($\xi=0$), both meridional flows contain two separation vortex bubbles (Figs. 2 and 3, $\xi=0$). Weak counter-rotation of the

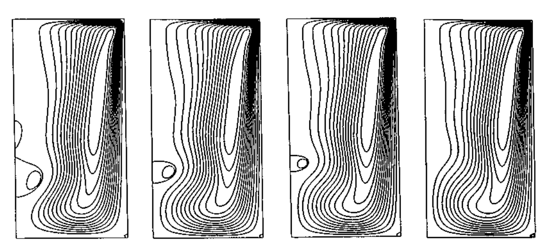

FIG. 2. Counter-rotating bottom. Streamlines. Here $\mathrm{Re}=2000$, $\gamma=2.0$, $0\geqslant\xi\geqslant-0.04$.

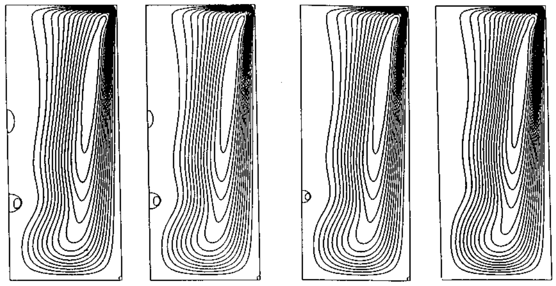

FIG. 3. Counter-rotating bottom. Streamlines. Here Re=2000, γ=2.5, $0 \geqslant \xi \geqslant -0.01$.

bottom eliminates both bubbles. In the case of $\gamma=2$ (Fig. 2) the upper separation bubble disappears when ξ reaches the value -0.02, and the lower one is suppressed when $\xi=-0.04$. When the aspect ratio is larger, even weaker counter-rotation is sufficient to eliminate the separation vortex bubbles. Thus, in the case $\gamma=2.5$ the upper and the lower separation bubbles disappear at $\xi=-0.005$ and -0.01, respectively (Fig. 3). The patterns of meridional flows for a further increase of the counter-rotation are similar to those illustrated in Fig. 1 for $\gamma=1.5$.

When the Reynolds number is higher (Re=3800, $\gamma=1.5$; Fig. 4) the influence of the counter-rotation on steady flows is different. In the case of rotating top and stationary bottom ($\xi=0$) the steady state does not contain the separation vortex bubble and it becomes unstable at much lower Reynolds number $\mathrm{Re}_{\mathrm{cr}} \approx 2700$. The counter-rotation of the bottom leads to the appearance of a separation vortex bubble at $\xi \approx -0.1$ in an unstable steady flow (Fig. 4, $\xi=-0.13$). The size of the separation bubble increases with the increase of the counter-rotation up to $\xi \approx -0.3$ ($\xi=-0.13$, -0.17, and -0.3). With a further decrease of ξ the size of the separation bubble increases ($\xi=-0.3$ and -0.4), and it merges with the counter-clockwise recirculation region. Referring to the stability diagram in Fig. 10(a) below, one can see that at Re=3800 the steady states $-0.134 \leqslant \xi \leqslant -0.127$ and $-0.350 \leqslant \xi \leqslant -0.225$ are stable, while other states are unstable. Thus in Fig. 4 the steady states at $\xi=-0.13$ and -0.3 are stable, the other states are unstable. This shows that at this Reynolds number, at which without counter-rotation ($\xi=0$) there is no vortex breakdown and the flow is unstable, a moderate counter-rotation ($\xi=-0.13$) induces a vortex breakdown and stabilizes the flow.

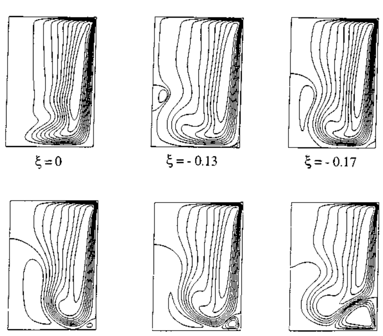

FIG. 4. Counter-rotating bottom. Streamlines. Here Re=3800, γ=1.5, $0 \geqslant \xi \geqslant -0.6$.

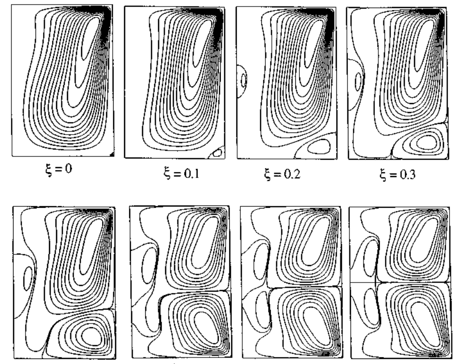

FIG. 5. Corotating bottom. Streamlines. Here Re=800, γ=1.5, $0 \leqslant \xi \leqslant 1$.

2. Corotating bottom

The effect of increasing corotation of the bottom is illustrated in Figs. 5–7 for $\gamma=1.5$ and different values of Re. Figure 5 (Re=800) shows that with a rotating top and stationary bottom ($\xi=0$) there is no vortex breakdown. Corotation of the bottom leads to the appearance of a separation vortex bubble in the flow when ξ reaches the value $\xi=0.2$. This is also in qualitative agreement with the experimental results of Roesner.[3,4] The size of the separation bubble increases with the increase of the corotation ($\xi=0.2$–0.5). The increasing corotation of the bottom induces a counterclockwise recirculation region that appears in the lower corner of the cylinder ($\xi=0.1$) and grows with the increase of ξ (from 0.1 to 0.5). When ξ becomes close to 1, the meridional flow tends to become antisymmetric with respect to the midplane of the cylinder. This leads to the appearance of the second separation vortex bubble ($\xi=0.8$, 0.9). The meridional flow becomes antisymmetric at $\xi=1$ and contains two antisymmetric separation bubbles that are attached to the axis.

Strong corotation may promote the vortex breakdown, even at significantly lower Reynolds numbers. This is illustrated in Fig. 6 for $\gamma=1.5$ and Re=400. The separation vortex bubble appears when ξ reaches the value of $\xi=0.9$. At $\xi=1$ the meridional flow contains the antisymmetric vortex breakdown similar to that shown in Fig. 5 for $\xi=1$.

The influence of corotation on a flow that has a vortex breakdown at $\xi=0$ is slightly different (Fig. 7). With the increase of ξ the separation vortex bubble grows and moves

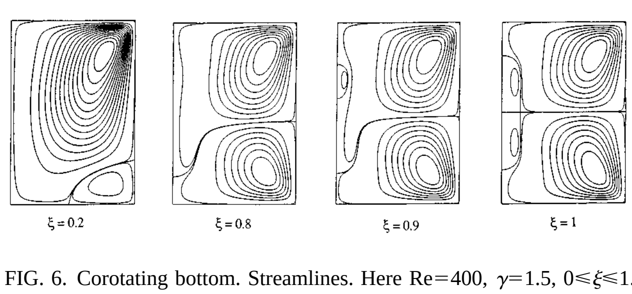

FIG. 6. Corotating bottom. Streamlines. Here Re=400, γ=1.5, $0 \leqslant \xi \leqslant 1$.

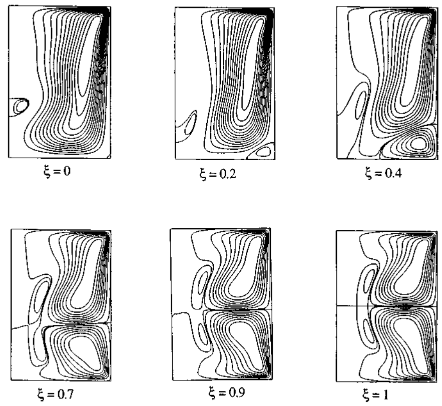

FIG. 7. Corotating bottom. Streamlines. Here Re=1500, $\gamma=1.5$, $0\leqslant\xi\leqslant1$.

downward, such that at $\xi=0.4$ the boundary of the recirculation zone is attached to the bottom. Two separation bubbles in the antisymmetric flow at $\xi=1$ are detached from the axis and form two antisymmetric vortex rings. The continuous change of shape of the recirculation zone in Fig. 7 shows that the ''usual'' vortex breakdown at $\xi=0$ and the vortex breakdown that is detached from the axis at $\xi=1$ are the results of the same vortex breakdown phenomenon and continuously transform one into another with the continuous change of ξ.

The appearance and evolution of the antisymmetric vortex breakdown for different Re in the case when the top and the bottom rotate with the same angular velocities ($\xi=1$) is shown in Fig. 8 for $\gamma=1.5$. Two antisymmetric separation vortex bubbles appear when the Reynolds number reaches a certain value (Re=400). With the increase of Re the size of the separation bubbles grows (Re=600). With a further increase of Re, the upper and the lower stagnation points on the axis of the cylinder move toward the middle stagnation point at $r=0$, $z=\gamma/2$ (Re=600, 700, and 800). When the Reynolds number becomes larger, the three stagnation points coincide and the recirculation zones detach from the axis (Re=1000).

Figure 9 shows the effect of corotation on the steady flow that contains two separation vortex bubbles at $\xi=0$. With a weak increase of the corotation both separation bubbles grow ($\xi=0.02$) until the two recirculation zones

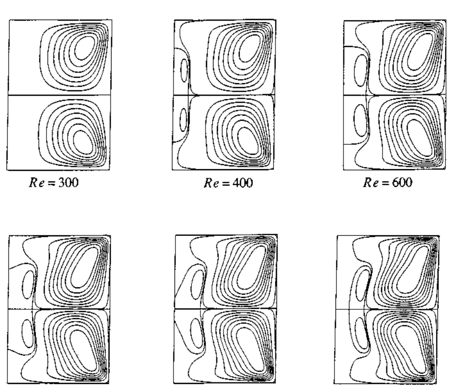

FIG. 8. Same corotation of the top and the bottom. Here $\xi=1$, $\gamma=1.5$, $300\leqslant\mathrm{Re}\leqslant1000$.

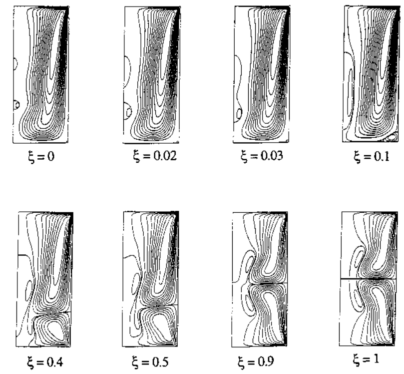

FIG. 9. Streamlines of meridional flow for Re=2000, $\gamma=2.5$, $0\leqslant\xi\leqslant1$.

merge ($\xi=0.03$) and form a relatively large single separation vortex bubble ($\xi=0.1$). The recirculation region initiated in the corner grows with the increase of the corotation (ξ varying from 0.1 to 0.4) until it merges with the vortex breakdown bubble, resulting in the existence of two recirculation fields ($\xi=0.5$). With a further increase of ξ the flow is finally deformed, at $\xi=1$, into four fields, two of which are symmetric detached bubbles.

The flows calculated for $\xi=1$ (Figs. 5–9) are in qualitative agreement with the experimental results of Spohn *et al.*[19] and with the numerical results of Valentine and Jahnke.[18]

B. Onset of oscillatory instability

The oscillatory instability was investigated for $\gamma=1.5$ and $-1\leqslant\xi\leqslant1$. It was found that the instability sets in as a result of a Hopf bifurcation[24] for all values of ξ. The direction of bifurcation[25] was checked for $\xi=-1$, 0, and 1 and was found to be supercritical.

1. Counter-rotating bottom

The influence of counter-rotation on the transition from steady to oscillatory flow was studied for $\gamma=1.5$. The dependence of the critical Reynolds number Re_{cr} on the rotation ratio ξ is shown in Fig. 10(a). Steady flows are stable below the solid curve and unstable above it. The corresponding dependence of the circular frequency of oscillations ω_{cr} on ξ is shown in Fig. 10(b). The curves $\mathrm{Re}_{cr}(\xi)$ and $\omega_{cr}(\xi)$ consist of four continuous branches corresponding to different dominant perturbations (different most unstable eigenmodes of the linearized problem). These eigenmodes become dominant at different values of the control parameters and abruptly replace each other at the points where the neutral curve $\mathrm{Re}_{cr}(\xi)$ has discontinuities in the slope. The almost vertical branch of the neutral curve $\mathrm{Re}_{cr}(\xi)$ located in the neighborhood of $\xi\approx-0.63$ corresponds to the onset of instability with a change of ξ rather than with the change of Re.

Figure 10(a) shows that the critical Reynolds number may be noticeably increased by a moderate counter-rotation. Thus, the critical Reynolds number increases from $\mathrm{Re}_{cr}=2724$ at $\xi=0$ to $\mathrm{Re}_{cr}=3957$ at $\xi=-0.27$. Stronger counter-rotation leads to nonmonotonic decrease of the critical Reynolds number, which reaches the value $\mathrm{Re}_{cr}=1646$ at $\xi=-1$.

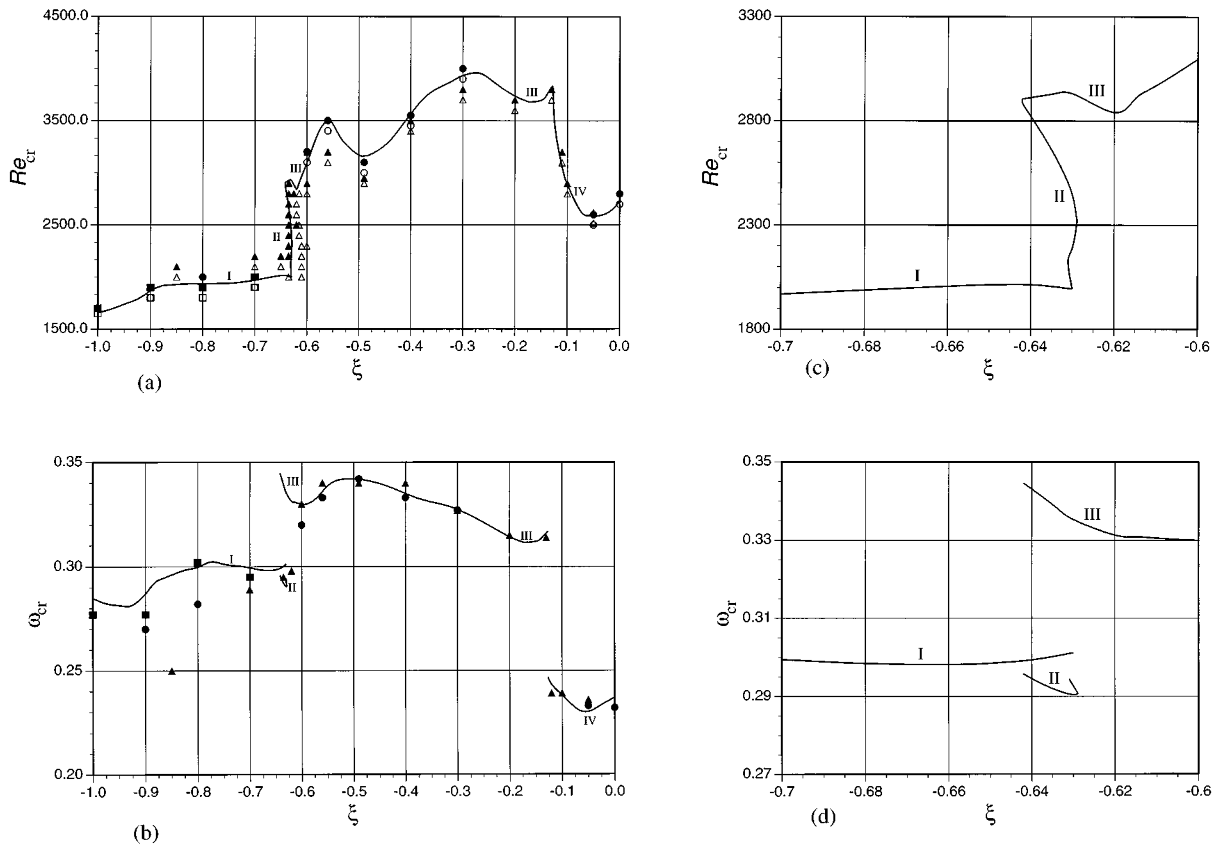

FIG. 10. Stability diagrams corresponding to the onset of oscillatory instability in a cylinder with rotating top and counter-rotating bottom. Here $\gamma=1.5$. Solid lines—results of the linear stability analysis (Galerkin method). Steady and unsteady states obtained by the solution of the full unsteady problem using the finite volume method are shown by △, ▲, for a 75×75 grid; ○, ●, for a 150×150 grid; □, ■, for a 200×200 grid. (a) $\mathrm{Re}_{\mathrm{cr}}$ vs ξ; (b) ω_{cr} vs ξ; (c) $\mathrm{Re}_{\mathrm{cr}}$ vs ξ, blowup of (a) for $-0.6\leqslant\xi\leqslant-0.7$; (d) ω_{cr} vs ξ, blowup of (b) for $-0.6\leqslant\xi\leqslant-0.7$.

Figure 10 also shows that the dependence $\mathrm{Re}_{\mathrm{cr}}(\xi)$ and $\omega_{\mathrm{cr}}(\xi)$ may be nonmonotonic and very sensitive to a small change of a control parameter, even along a continuous branch of the neutral curve. This behavior of the critical parameters was verified by straightforward solution of the full unsteady problem using the finite volume method with 75×75, 150×150, and 200×200 stretched grids [Figs. 10(a) and 10(b)]. It is seen that the nonmonotonic behavior of the curves $\mathrm{Re}_{\mathrm{cr}}(\xi)$ and $\omega_{\mathrm{cr}}(\xi)$ can be reproduced also by the finite volume method. Results of both numerical methods are close when $\xi>-0.7$. In the interval $-1\leqslant\xi\leqslant-0.7$ the frequency of oscillations calculated by the finite volume method converges slowly, but with the refinement of the mesh becomes closer to the result of the spectral method.

The four branches of the curves $\mathrm{Re}_{\mathrm{cr}}(\xi)$ and $\omega_{\mathrm{cr}}(\xi)$ (labeled I–IV in Fig. 10) correspond to four different modes of the perturbation. Examples of steady flows at the critical values of parameters and corresponding perturbations are shown in Fig. 11. Each plot in Fig. 11 is arranged in the following way: solid curves show isolines of the streamfunction ψ and the azimuthal moment $\mathscr{M}_\varphi$; dashed lines show isolines of the modulus of the most unstable linear modes of perturbations of the functions ψ and $\mathscr{M}_\varphi$. The left part of each plot corresponds to the azimuthal moment $\mathscr{M}_\varphi$ and its perturbation (perturbation of the azimuthal component of the flow). The right part of each plot corresponds to the streamfunction ψ and its perturbation (perturbation of the meridional component of the flow). The axis of the cylinder is shown by a vertical line in the middle of each plot.

Figure 11(a) corresponds to the branch of the neutral curve that starts at $\xi=-1$ and ends at $\xi\approx-0.63$ (branch I). The perturbations of ψ and $\mathscr{M}_\varphi$ have a global maximum on

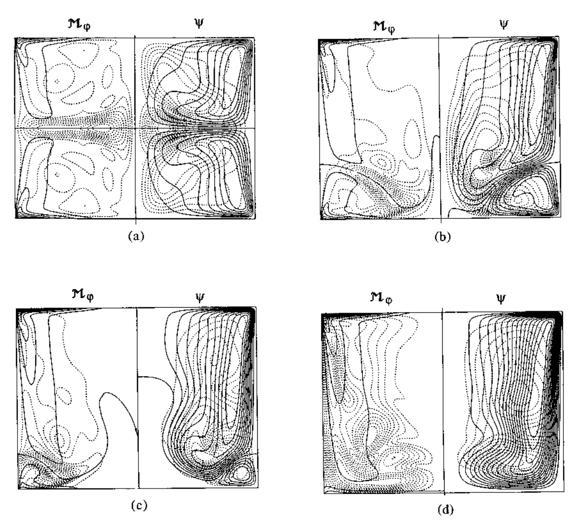

FIG. 11. Isolines of the rotational moment $\mathscr{M}_\varphi$ (the left part of each plot) and the streamfunction ψ (the right part of each plot) at the critical point (solid lines) and isolines of the corresponding perturbations (dashed lines). Counter-rotation, $\gamma=1.5$. (a) $\xi=-1$, $\mathrm{Re}_{\mathrm{cr}}=1646$; (b) $\xi=-0.64$, $\mathrm{Re}_{\mathrm{cr}}=2905$; (c) $\xi=-0.49$, $\mathrm{Re}_{\mathrm{cr}}=3158$; (d) $\xi=-0.05$, $\mathrm{Re}_{\mathrm{cr}}=2585$.

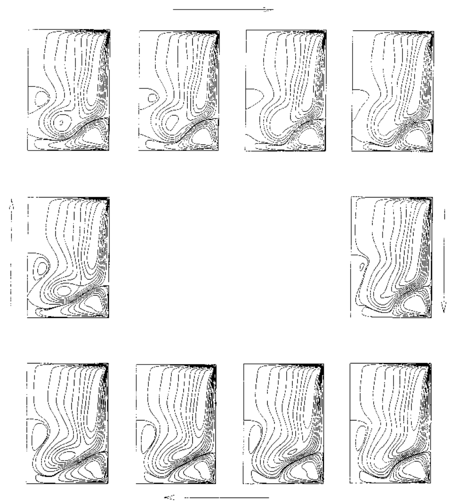

FIG. 12. Instantaneous streamlines of the meridional flow plotted for equal time intervals 0.1 T covering the complete period $T=19.21$. $\gamma=1.5$, $\xi=-0.6$, and Re=3200. Calculation with the finite volume method using a 75×75 stretched grid.

the isolines corresponding to $\psi=0$ and $\mathscr{M}_\varphi=0$. In the case $\xi=-1$, shown in Fig. 11(a), the isolines $\mathscr{M}_\varphi=0$ and $\psi=0$ coincide with the midplane of the cylinder; for other values of ξ they do not. Similar patterns of the perturbation are obtained at the next, almost vertical, branch of the neutral curve (branch II). The example is shown in Fig. 11(b). The perturbations of both functions have a global maximum on the isolines $\mathscr{M}_\varphi=0$ and $\psi=0$. Generally, one can say that these branches of the neutral curve correspond to an instability that sets in at the boundary separating two distinct regions: the region of positive rotation of the fluid with its clockwise recirculation region and the region of negative rotation of the fluid with its counterclockwise recirculation region.

Examples of the perturbations characteristic for the next two branches of the neutral curve [Fig. 10(a)], which correspond to the intervals $-0.64\leqslant\xi\leqslant-0.13$ (branch III) and $-0.13\leqslant\xi\leqslant0$ (branch IV) are shown in Figs. 11(c) and 11(d). In the case $\xi=-0.49$ [Fig. 11(c)] the perturbation of $\mathscr{M}_\varphi$ still has a global maximum on the isoline $\mathscr{M}_\varphi=0$, but the largest value of the perturbation of ψ is located inside the largest recirculation region. The pattern of the perturbation of $\mathscr{M}_\varphi$ becomes completely different on the next branch of the neutral curve [Fig. 11(d)]. The onset of instability along these two branches is characterized by a rapid growth of the perturbation of $\mathscr{M}_\varphi$ along the sidewall and the bottom of the cylinder. Similar patterns of perturbations were reported by Gelfgat *et al.*[11] in the case of $\xi=0$ and varying γ.

Oscillations of the meridional flow in a slightly supercritical state are illustrated in Fig. 12 for $\xi=-0.6$. The pulsations of the meridional flow in this case [branch III in Fig. 10(a)] lead to the appearance of a weak separation vortex bubble that exists during approximately one-half of a period. During the other half of a period the separation bubble merges with the region of counterclockwise meridional circulation. A similar plot (not shown here) of instantaneous streamlines for a case on a different branch of the neutral curve [$\xi=-0.7$, branch I in Fig. 10(a)] shows only a weak pulsation of both recirculation regions, without an instantaneous separation bubble.

2. Corotating bottom

The influence of corotation on the onset of the oscillatory instability was studied for the same aspect ratio $\gamma=1.5$. The corresponding relations $\mathrm{Re}_{cr}(\xi)$ and $\omega_{cr}(\xi)$ are shown in Figs. 13(a) and 13(b). In some aspects the influence of corotation is similar to that of counter-rotation.

(i) There is a part of the neutral curve, located at $\xi\approx0.55$, which corresponds to the onset of instability with increasing of ξ rather than with increasing of Re (branches VI and VIII). This part of the neutral curve and the corresponding part of the relation $\omega_{cr}(\xi)$ are expanded in Figs. 13(c) and 13(d).

(ii) A certain corotation may significantly increase the critical Reynolds number. On the whole, all the values of the critical Reynolds number for $\xi>0$ are larger than the value of Re_{cr} at $\xi=0$. The neutral curve $\mathrm{Re}_{cr}(\xi)$ has two sharp maxima. The first maximum corresponds to the rapid increase of Re_{cr} from $\mathrm{Re}_{cr}=2724$ at $\xi=0$ to $\mathrm{Re}_{cr}=3847$ at $\xi=0.09$. The second maximum $\mathrm{Re}_{cr}=4575$ is located at $\xi=0.56$. This is the largest value of Re_{cr} in the whole interval $-1\leqslant\xi\leqslant1$.

The nonmonotonous behavior of the curves $\mathrm{Re}_{cr}(\xi)$ and $\omega_{cr}(\xi)$ was reproduced by the solution of the full unsteady problem using the finite volume method. The number of nodes of the stretched grid varied from 75×75 to 200×200 [Figs. 13(a) and 13(b)]. Details of these calculations are described in the Appendix.

There exist several branches of the curves $\mathrm{Re}_{cr}(\xi)$ and $\omega_{cr}(\xi)$ corresponding to different most unstable linear modes of the steady flow (Fig. 13). Examples of the patterns of the most dominant perturbations and flows at the critical values of parameters are shown in Fig. 14. The flows and the perturbations are shown in Fig. 14 in the same way as for the counter-rotation in Fig. 11.

The patterns of the perturbations corresponding to the two branches located in the intervals $0\leqslant\xi\leqslant0.05$ (branch IV) and $0.05\leqslant\xi\leqslant0.09$ (branch V) are similar to those obtained for $\xi=0$ and described by Gelfgat *et al.*[11] Figures 14(a) and 14(b) correspond to the next branch of the neutral curve (branch VI), which starts at $\xi\approx0.1$ and continues until $\xi\approx0.56$, with a short break in the interval $0.3\leqslant\xi\leqslant0.31$ (branch VII) [Fig. 13(a)]. The maximum of the perturbations of ψ is located in the lower part of the main clockwise recirculation region while the maxima of the perturbation of $\mathscr{M}_\varphi$ are located in the area where rotation is relatively weak. Comparison of Figs. 14(a) and 14(b) shows that with the growth of ξ the maxima of the perturbation of $\mathscr{M}_\varphi$ are shifted upward, together with the region where the axial distributions of $\mathscr{M}_\varphi$ for a fixed radius reach their minimum.

Figures 14(c)–14(e) illustrate flows and perturbations that are characteristic for strong corotation, which corresponds to the branch of the neutral curve located in the interval $0.585\leqslant\xi\leqslant1$ [branch X in Fig. 13(a)]. At the beginning of this branch [Fig. 14(c), $\xi=0.6$] the perturbations of ψ and $\mathscr{M}_\varphi$ are strongest in the region where rotation is weak [the

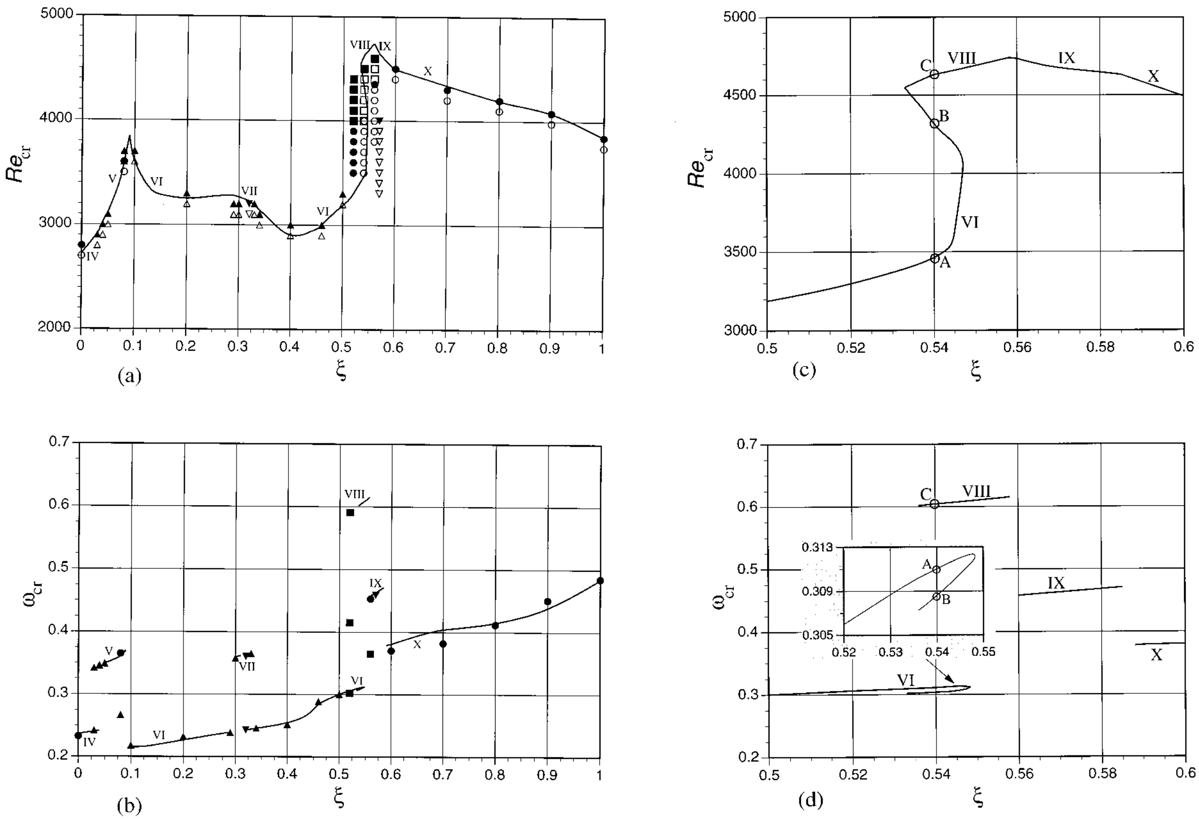

FIG. 13. Stability diagrams corresponding to the onset of oscillatory instability in a cylinder with a rotating top and a corotating bottom. Here $\gamma=1.5$. Solid lines—results of the linear stability analysis (Galerkin method). Steady and unsteady states obtained by the solution of the full unsteady problem using the finite volume method are shown by △, ▲, for a 75×75 grid; ▼, ▼, for a 100×100 grid; ○, ●, for a 150×150 grid; □, ■, for a 200×200 grid. (a) Re_{cr} vs ξ; (b) ω_{cr} vs ξ, (c) Re_{cr} vs ξ, blowup of (a) for $0.5\leqslant\xi\leqslant0.6$; (d) ω_{cr} vs ξ, blowup of (b) for $0.5\leqslant\xi\leqslant0.6$.

left part of Fig. 14(c)] and where the isoline $\psi=0$, separating clockwise and counterclockwise meridional circulations, is located. This is analogous (but not identical) to the case of strong counter-rotation shown in Figs. 11(a) and 11(b). With the increase of ξ up to $\xi=1$, the perturbation of ψ is characterized by two maxima located in the clockwise and the counterclockwise recirculation regions. The pattern of the perturbation of $\mathscr{M}_\varphi$ is very different from the previous cases and has a global maximum in the same place where the separation vortex bubbles are located. The whole structure of the flow and the perturbation become reflection symmetric with respect to the plane $z=\gamma/2$ at $\xi=1$. This leads to the conclusion that the oscillatory instability at $\xi=1$ sets in without a break of the reflection symmetry, which is in agreement with the result of Lopez[20] obtained for $\xi=1$ and $\gamma=3$ ($\gamma_{\mathrm{Lopez}}=\gamma/2=1.5$). The solution of the unsteady problem by the finite volume method (see Fig. 18) also shows that the reflection symmetry is preserved in a slightly supercritical state.

The symmetric structure of the flow and the perturbation at $\xi=1$ allowed us to verify the result by taking into consideration one-half of the cylinder and imposing the boundary conditions of symmetry at the lower horizontal boundary. Close values of Re_{cr} and ω_{cr} were obtained for both nonsymmetric and symmetric models (for details see the Appendix and Table I). The patterns of the flow and perturbations obtained for the symmetric model are shown in Fig. 14(e). It is seen that the patterns of the flow and the perturbations in Figs. 14(d) and 14(e) are similar. However, it is clear that the spatial resolution of the numerical method is much better in the symmetric case, where only one-half of the flow region is taken into consideration.

The abrupt changes of the perturbations when one dominant mode is replaced by another one are illustrated in Figs. 15 and 16. Figure 15 corresponds to the changes of the dominant mode in the neighborhood of $\xi=0.3$, which is seen in Fig. 13(b) as the sudden jump of the critical frequency from $\omega_{cr}=0.239$ to $\omega_{cr}=0.362$ at $\xi=0.3$ and then back to $\omega_{cr}=0.243$ at $\xi=0.32$. Figure 15 shows that patterns of the perturbations at $\xi=0.29$ and $\xi=0.32$ are similar, but are noticeably different at $\xi=0.3$. The instability in most of the interval $0.1\leqslant\xi\leqslant0.56$ is caused by the same mode of the perturbation [also see Figs. 14(a) and 14(b)], except the short interval $0.3\leqslant\xi\leqslant0.32$ where the characteristics of the instability (amplitude and frequency of oscillations) are different.

Note that at $\xi=0.54$ there exist three distinct critical points with different critical frequencies ω_{cr}, as indicated by A, B, and C in Figs. 13(c) and 13(d). The isolines of perturbations corresponding to these three points are shown in Fig. 16. With the increase of Re [see Fig. 13(c)] the steady flow loses its stability at Re=3463, then becomes stable at Re =4326 and finally loses the stability at Re=4632. Comparison of the perturbations plotted in Fig. 16 shows that two critical points illustrated in Figs. 16(a) and 16(b) belong to

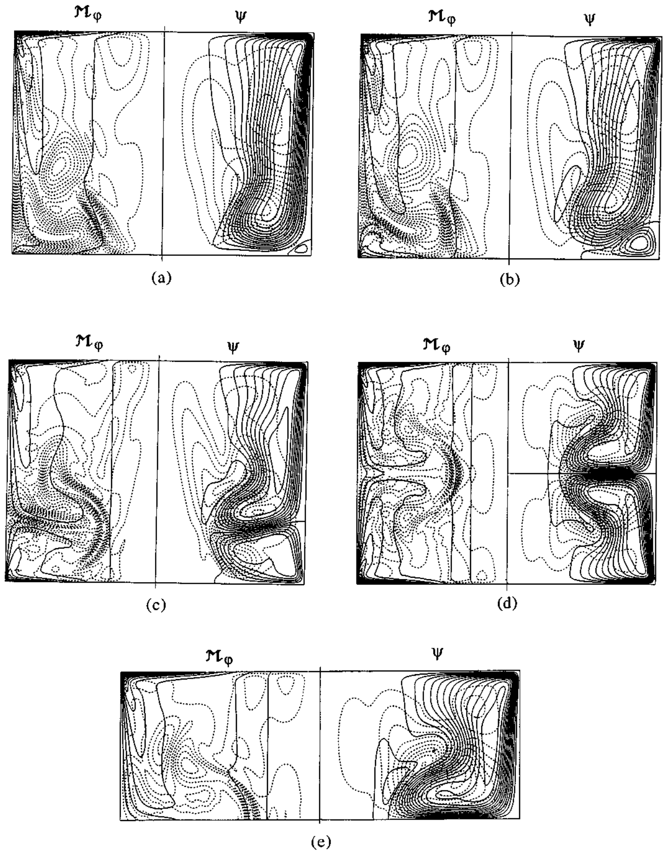

FIG. 14. The same as Fig. 11. Corotation, $\gamma=1.5$. (a) $\xi=0.2$, $\mathrm{Re}_{\mathrm{cr}}=3249$; (b) $\xi=0.4$, $\mathrm{Re}_{\mathrm{cr}}=2905$; (c) $\xi=0.6$, $\mathrm{Re}_{\mathrm{cr}}=4493$; (d) $\xi=1$, $\mathrm{Re}_{\mathrm{cr}}=3843$; (e) $\xi=1$, $\mathrm{Re}_{\mathrm{cr}}=3845$, symmetric case.

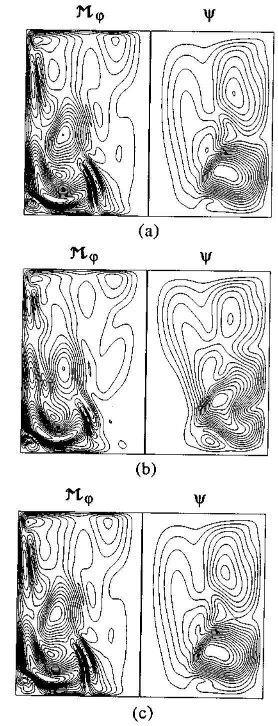

FIG. 15. Changes in the patterns of the perturbations of $\mathscr{M}_\varphi$ (the left part of each plot) and of ψ (the right part of each plot) in the neighborhood of $\xi=0.3$. (a) $\xi=0.29$, $\mathrm{Re}_{\mathrm{cr}}=3278$; (b) $\xi=0.3$, $\mathrm{Re}_{\mathrm{cr}}=3265$; (c) $\xi=0.32$, $\mathrm{Re}_{\mathrm{cr}}=3228$.

the same branch of the neutral curve [branch I in Figs. 13(c) and 13(d)], while the third point belongs to another branch [branch II in Figs. 13(c) and 13(d)]. Similar examples of the abrupt changes in the patterns of perturbations can be made for all other points, where the neutral curve $\mathrm{Re}_{\mathrm{cr}}(\xi)$ has discontinuities in the slope, and where the relation $\omega_{\mathrm{cr}}(\xi)$ has abrupt jumps.

Since the critical values on the branch of the neutral curve $0.57\leqslant\xi\leqslant1$ showed the slowest convergence (see the Appendix and Table I), the results were verified by the solution of the full unsteady problem using the finite volume

TABLE I. Convergence study for the critical parameters. Here $\gamma=1.5$.

$\gamma=1.5$		30×30 basis functions	32×32 basis functions	34×34 basis functions	36×36 basis functions	38×38 basis functions	40×40 basis functions
$\xi=-1$	$\mathrm{Re}_{\mathrm{cr}}$	1700	1669	1656	1649	1646	1644
	ω_{cr}	0.2887	0.2859	0.2848	0.2842	0.2839	0.2837
$\xi=-0.6$	$\mathrm{Re}_{\mathrm{cr}}$	3096	3107	3105	3105	3105	3105
	ω_{cr}	0.3300	0.3295	0.3293	0.3291	0.3290	0.328 95
$\xi=-0.27$	$\mathrm{Re}_{\mathrm{cr}}$	3957	3957	3957	3957	3957	3957
	ω_{cr}	0.323 86	0.323 85	0.323 85	0.323 86	0.323 86	0.323 86
$\xi=0$	$\mathrm{Re}_{\mathrm{cr}}$	2724	2724	2724	2724	2724	2724
	ω_{cr}	0.236 748	0.236 749	0.236 752	0.236 754	0.236 753	0.236 754 5
$\xi=0.29$	$\mathrm{Re}_{\mathrm{cr}}$	3279	3278	3278	3278	3278	3278
	ω_{cr}	0.239 09	0.239 09	0.239 09	0.239 10	0.239 10	0.239 10
$\xi=0.6$	$\mathrm{Re}_{\mathrm{cr}}$	4532	4544	4557	4549	4522	4493
	ω_{cr}	0.4822	0.4805	0.4798	0.3878	0.3824	0.3806
$\xi=0.8$	$\mathrm{Re}_{\mathrm{cr}}$	4247	4176	4265	4398	4452	4191
	ω_{cr}	0.5645	0.3776	0.3845	0.5550	0.5511	0.4148
$\xi=1$	$\mathrm{Re}_{\mathrm{cr}}$	3218	3369	3528	3731	3837	3845
non-symmetric	ω_{cr}	0.6018	0.5936	0.5877	0.5814	0.4527	0.4603
$\xi=1$	$\mathrm{Re}_{\mathrm{cr}}$	3846	3843	3843	3842	3843	3845
symmetric	ω_{cr}	0.4845	0.4842	0.4840	0.4840	0.4840	0.4840

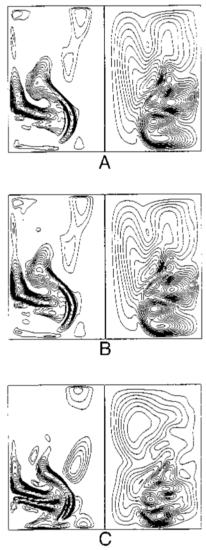

FIG. 16. Changes in the patterns of the perturbations of $\mathscr{M}_\varphi$ (the left part of each plot) and of ψ (the right part of each plot) at $\xi=0.54$ corresponding to three values of Re_{cr}. (a) $Re_{cr}=3463$; (b) $Re_{cr}=4326$; (c) $Re_{cr}=4632$.

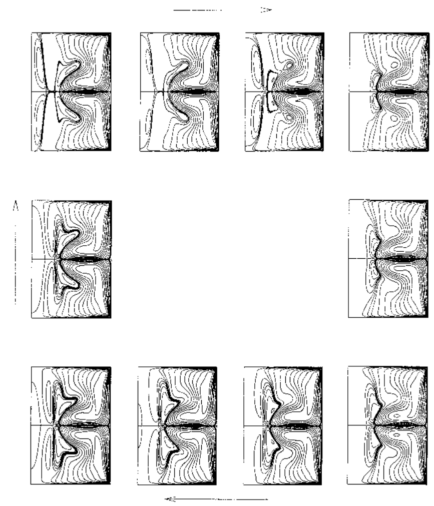

FIG. 18. Instantaneous streamlines of the meridional flow plotted for equal time intervals $0.1T$ covering the complete period $T=13.01$. $\gamma=1.5$, $\xi=1$, and Re=3845. Calculation with the finite volume method using a 150×150 stretched grid.

method with a 150×150 stretched grid. Figs. 13(a) and 13(b) show that the obtained results are in agreement both for critical values of the Reynolds number and the critical frequency. Examples of the calculated slightly supercritical flows are shown in Figs. 17 and 18.

In the case $\xi=0.8$ (Fig. 17) the oscillations of the two main meridional recirculation regions are followed by a rapid change of the vortical structure near the axis of the cylinder. During one period of oscillations one can see the appearance and disappearance of different separation vortex bubbles. Some of these are attached to the axis and others are detached. The structure becomes more regular in the symmetric case $\xi=1$ (Fig. 18, symmetry was not imposed *a priori* in the computations). In this case two pulsating pairs of attached and detached separation vortex bubbles are clearly seen. It should be noticed that the simultaneous coexistence of the detached and attached vortex breakdowns was not observed in steady states. This leads to the conclusion that such a coexistence is a feature of the oscillatory states only.

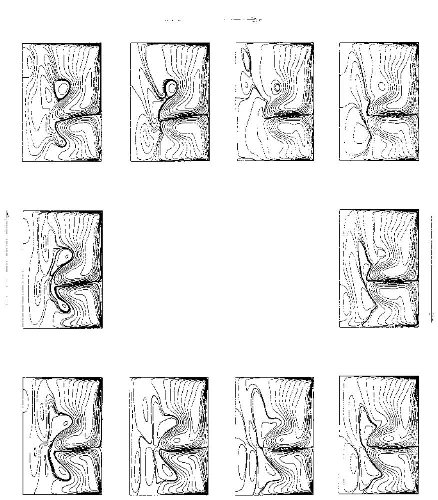

FIG. 17. Instantaneous streamlines of the meridional flow plotted for equal time intervals $0.1T$ covering the complete period $T=15.25$. $\gamma=1.5$, $\xi=0.8$, and Re=4200. Calculation with the finite volume method using a 150×150 stretched grid.

IV. CONCLUSIONS

A weak counter-rotation of the bottom may suppress the vortex breakdown that exists in a cylinder with a rotating top and a stationary bottom. The larger the aspect ratio of the cylinder the weaker the counter-rotation necessary to suppress the vortex breakdown. On the other hand, a certain counter-rotation may induce the vortex breakdown and stabilize steady flows at relatively large values of the Reynolds number for which, in the case of the stationary bottom, no vortex breakdown exists in unstable steady states.

Weak corotation of the bottom of the cylinder leads to the appearance of vortex breakdown at lower values of the Reynolds number than in the case of a stationary bottom. Stronger corotation may lead to the detachment of the separation vortex bubble from the axis of the cylinder and formation of two vortex rings. It was shown that the meridional flow with a single separation bubble, characteristic for the case of a stationary bottom, and the meridional flow with antisymmetric separation vortex rings, characteristic for corotation of the top and the bottom with the same angular velocity, continuously transform one into the other with a continuous change of the rotation ratio.

The stability of steady flows, onset of the oscillatory instability, and slightly supercritical oscillatory states were studied for a fixed aspect ratio of the cylinder $\gamma=1.5$. It was found that the oscillatory instability sets in due to a Hopf bifurcation in all the possible cases of co- and counter-rotation. It was shown that the oscillatory instability may set in, either with an increase of the Reynolds number or with a change of the rotation ratio. The corresponding stability diagrams in the plane of the control parameters (Re,ξ) were obtained yielding also the dependence of the critical frequency ω_{cr} on the rotation ratio. It was shown that the neutral curve $\mathrm{Re}_{cr}(\xi)$ and the curve $\omega_{cr}(\xi)$ consist of several continuous branches corresponding to several different dominant perturbations of the flow, which are defined by distinct eigenmodes of the linearized problem. Characteristic patterns of the most dominant perturbations were reported and discussed. It was found that both co- and counter-rotation of the bottom may stabilize the steady flow and significantly increase the critical Reynolds number. The strongest stabilization takes place when the rotation ratio reaches the values $\xi=0.56$ and $\xi=-0.27$ for co- and counter-rotation, respectively.

Investigation of the slightly supercritical states showed good agreement between the results of the linear stability analysis (using the spectral Galerkin method) and the results of the numerical solution of the full unsteady problem (using the finite volume method). It was found that in the case of strong corotation the vortex breakdowns attached to and detached from the axis may exist simultaneously in slightly supercritical oscillatory states.

ACKNOWLEDGMENTS

This research was supported by the Center for Absorption in Science, Ministry of Immigrant Absorption, State to Israel (to A. Gelfgat), by the Y. Winograd Chair of Fluid Mechanics and Heat Transfer at the Technion, and by the Fund for the Promotion of Research at the Technion.

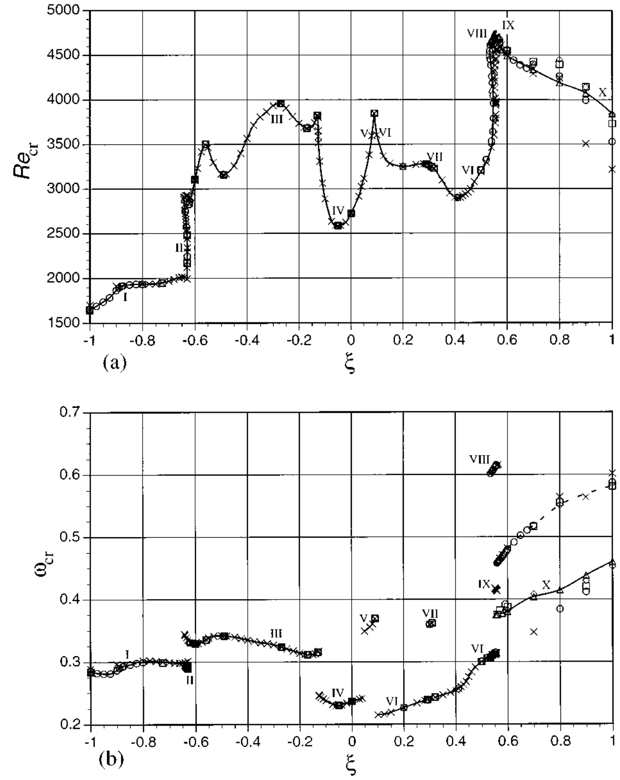

FIG. 19. Critical parameters obtained with a different number of basis functions. (a) Re_{cr} vs ξ, (b) ω_{cr} vs ξ. $\times$, 30$\times$30 Galerkin functions; $\bigcirc$, 34$\times$34 Galerkin functions; $\square$, 36$\times$36 Galerkin functions; $\diamondsuit$, 38$\times$38 Galerkin functions; and $\triangle$, 40$\times$40 Galerkin functions.

APPENDIX: DEPENDENCE OF RESULTS ON THE NUMERICAL DISCRETIZATION

The calculations of steady states do not cause any numerical difficulties. The steady states shown in Figs. 1–9 were calculated, both with the Galerkin spectral method and with the finite volume method. The number of basis functions in the Galerkin method varied from 24$\times$24 to 30$\times$30. The number of nodes in the stretched finite volume grid varied from 50$\times$50 to 100$\times$100. Comparison of results obtained with the finest discretizations showed that the calculated values of the streamfunction and the azimuthal velocity differ by less than 1%. Correct patterns of the flow were obtained also with coarser discretizations.

The critical parameters Re_{cr} and ω_{cr} calculated with different numbers of basis functions in the truncated Galerkin series are shown in Fig. 19 for the whole interval $-1\leqslant\xi\leqslant1$. The largest number of the basis functions was 40$\times$40 in the Galerkin series used for the approximations of the meridional and the azimuthal components of the flow (see Gelfgat *et al.*[11] for details). Thus, the largest total number of degrees of freedom for the Galerkin method was 3200.

The convergence of the critical parameters for different values of the rotation ratio ξ is shown in Table I. It was shown by Gelfgat *et al.*[11] that the use of 24$\times$24 basis functions in the Galerkin series gives three correct digits of the critical Reynolds number and five correct digits of the critical frequency for the case $\xi=0$, $\gamma=1.5$ (the values of Re_{cr} and ω_{cr} are reported in Table I). However, the convergence for large $|\xi|$ is slower, especially for $\xi\geqslant0.6$. The most detailed comparison reported in Fig. 19 is done for calculations with 30$\times$30 and 34$\times$34 basis functions. The results for these two discretizations coincide in the interval $-0.8\leqslant\xi\leqslant0.5$. For $-1\leqslant\xi\leqslant-0.8$ and $0.5\leqslant\xi\leqslant0.6$ the 40$\times$40 discretization gives only two correct digits of the critical parameters.

The critical values in the interval $0.6\leqslant\xi\leqslant1$ are most sensitive to discretization. It was found that there are two distinct eigenvalues in this interval, which change their signs at very close values of the Reynolds number. Two distinct curves of $\omega_{cr}(\xi)$ for $0.6\leqslant\xi\leqslant1$ are shown in Fig. 19(b). Besides this, the convergence of the critical Reynolds number is much slower than it was for smaller values of ξ, such that for $\xi\geqslant0.7$ the use of 40$\times$40 basis functions is not enough to ensure the convergence. However, with an increasing number of basis functions the intervals between sequentially obtained Re_{cr} decrease.

More exact conclusions about the onset of instability in the interval $0.6\leqslant\xi\leqslant1$ were drawn from the solution of the full unsteady problem using the finite volume method with a 150$\times$150 stretched grid. The slightly supercritical oscillatory state at $\xi=1$ showed that the instability sets in without a break of the reflection symmetry with respect to the plane $z=\gamma/2$. This allowed us to repeat the calculations with the Galerkin method for only one-half of the cylinder and to obtain the converged values of Re_{cr} and ω_{cr} at $\xi=1$ (see Table I). Further calculations with the finite volume method for $\xi=0.9$, 0.8, 0.7, and 0.6 showed that the critical Reynolds number is localized correctly [see Fig. 13(a)], and that the perturbation with lower ω_{cr} [see Fig. 19(b) for $0.6\leqslant\xi\leqslant1$] is dominant. Because of this the branch with lower ω_{cr} is shown by a solid line in Figs. 13(b) and 19(b), and the branch with larger ω_{cr} is shown by a dashed line in Fig. 19(b) only.

A series of time-dependent calculations with the finite volume method was carried out to verify the rapid increase of the critical Reynolds number at $\xi \approx -0.63$ and $\xi \approx 0.55$ [Figs. 10(a) and 13(a)]. At $\xi \approx -0.63$ the almost vertical branch of the neutral curve, calculated by the spectral method, is well reproduced with the use of a 75×75 grid [the corresponding Re_{cr} is located between the symbols $\triangle$ and $\blacktriangle$, Fig. 10(a)]. Much worse convergence was observed in the vicinity of $\xi \approx 0.55$. Thus, calculations with 100×100, 150×150, and 200×200 grids at $\xi = 0.56$ and 0.57 [Fig. 13(a)] showed that the critical Reynolds number grows with the increase of the number of grid nodes. Using 150×150 and 200×200 grids we succeeded to localize the almost vertical branch of the neutral curve (the corresponding Re_{cr} is located between the symbols $\square$, $\bigcirc$ and $\blacksquare$, $\bullet$, Fig. 13(a)]. Compared to the almost vertical branch calculated by the spectral method, the same branch calculated by the finite volume method is shifted toward lower values of the rotation ratio (it is located between $\xi = 0.52$ and $\xi = 0.54$). However, as it was noticed above, in this case one cannot be sure of the convergence of the finite volume method.

Slow convergence of the finite volume method was also observed near points where the neutral curves $Re_{cr}(\xi)$ have breaks in the slope and an abrupt change of the critical frequency takes place [Figs. 10(a), 10(b) and Figs. 13(a), 13(b)]. Thus, calculations in the interval $0 \leqslant \xi \leqslant 0.5$ with the 75×75 finite volume grid showed that the corresponding critical parameters are close to those calculated by the spectral method almost everywhere, except near break points at $\xi = 0.08$ and 0.32. For example, at $\xi = 0.08$ the frequency of oscillations obtained on a 75×75 finite volume grid does not agree with the result of the spectral method [Fig. 13(b)]. To obtain the correct result, which agrees with the converged calculations of the spectral method, it was necessary to use 150×150 nodes [Fig. 13(b)]. At the same time the results of the calculations using 75×75 nodes at $\xi = 0.05$ and $\xi = 0.1$ are in good agreement with the results of the spectral method.

A slow convergence of the frequency of oscillations calculated by the finite volume method was observed also in the interval $-1 \leqslant \xi \leqslant -0.7$ [Fig. 10(b)]. However, a comparison of results obtained using the 100×100, 150×150, and 200×200 nodes shows that with the refinement of the mesh the values of the critical frequency become closer to those calculated by the spectral method.

[1] H. U. Vogel, ''Rückströmungsblasen in Drallströmungen,'' in *Festschrift zum 50–Jährigen Bestehen des MPI für Strömungsforschung* (Hubert, Göttingen, 1975), p. 263.

[2] M. P. Escudier, ''Observation of the flow produced in a cylindrical container by a rotating endwall,'' Exp. Fluids **2**, 189 (1984).

[3] K. G. Roesner, ''Recirculation zones in a cylinder with rotating lid,'' in *Proceedings of the IUTAM Symposium on Topological Fluid Mechanics*, edited by A. Tsinober and H. K. Moffat (University of Cambridge, Cambridge, 1989), p. 699.

[4] P. Z. Bar-Yoseph, A. Solan, and K. G. Roesner, ''Recirculation zones in a cylinder with rotating lid,'' Z. Angew. Math. Mech. **70**, 442 (1990).

[5] C. Westergaard, P. Buchhave, and J. N. Sørensen, ''PIV measurements of turbulent and chaotic structures in a rotating flow using an optical correlator,'' in *Laser Techniques and Applications in Fluid Mechanics*, edited by R. J. Adrian (Springer-Verlag, Berlin, 1993), p. 243.

[6] H. J. Lugt and M. Abboud, ''Axisymmetric vortex breakdown with and without temperature effects in a container with a rotating lid,'' J. Fluid Mech. **179**, 179 (1987).

[7] J. N. Sørensen and O. Daube, ''Direct simulation of flow structures initiated by a rotating cover in a cylindrical vessel,'' in *Advances in Turbulence*, edited by H. H. Fernholz and H. E. Fielder (Springer-Verlag, Berlin, 1989), p. 383.

[8] J. M. Lopez, ''Axisymmetric vortex breakdown. Part 1: Confined swirling flow,'' J. Fluid Mech. **221**, 533 (1990).

[9] J. M. Lopez and A. D. Perry, ''Axisymmetric vortex breakdown. Part 3: Onset of periodic flow and chaotic advection,'' J. Fluid Mech. **234**, 449 (1992).

[10] J. N. Sørensen and E. A. Christensen, ''Direct numerical simulation of rotating fluid flow in a closed cylinder,'' Phys. Fluids **7**, 764 (1995).

[11] A. Yu. Gelfgat, P. Z. Bar-Yoseph, and A. Solan, ''Stability of confined swirling flow with and without vortex breakdown,'' J. Fluid Mech. **311**, 1 (1996).

[12] A. Yu. Gelfgat, P. Z. Bar-Yoseph, and A. Solan, ''Numerical investigation of a confined swirling flow in a cylinder with rotating top and bottom by the Galerkin spectral method,'' *Proceedings of the 6th International Symposium Computational Fluid Dynamics*, Lake Tahoe, Nevada, 4–8 September, 1995, p. 355.

[13] P. Z. Bar-Yoseph, K. G. Roesner, and A. Solan, ''Vortex breakdown in the polar region between rotating spheres,'' Phys. Fluids A **4**, 1677 (1992).

[14] P. Z. Bar-Yoseph, ''Multiple flow patterns and vortex breakdown in rotating flows,'' Comput. Fluid Dyn. J. **3**, 273 (1994).

[15] P. Z. Bar-Yoseph, ''Computational investigation of confined rotating flows—A continuous challenge,'' Chapter in *Computational Fluid Dynamics*, edited by D. Leutloff and R. C. Srinivastava (Springer-Verlag, Berlin, 1995), p. 257.

[16] P. Z. Bar-Yoseph and Yu. Kryzhanovski, ''On the validity of power law models in the prediction of vortex breakdown phenomena,'' Comput. Fluid Dyn. J. (in press).

[17] P. Z. Bar-Yoseph and Yu. Kryzhanovski, ''Non-Newtonian effects on axisymmetric vortex breakdown in confined swirling flows,'' J. Non-Newt. Fluid Mech. (in press).

[18] D. T. Valentine and C. C. Jahnke, ''Flows induced in a cylinder with both walls rotating,'' Phys. Fluids A **6**, 2702 (1994).

[19] A. Spohn, M. Mory, and E. J. Hopfinger, ''Observations of vortex breakdown in an open cylindrical container with a rotating bottom,'' Exp. Fluids **14**, 70 (1993).

[20] J. M. Lopez, ''Unsteady swirling flow in an enclosed cylinder with reflection symmetry,'' Phys. Fluids, **7**, 2700 (1995).

[21] A. Yu. Gelfgat, P. Z. Bar-Yoseph, and A. Solan, ''Confined swirling flow simulation using spectral Galerkin and finite volume methods,'' *Proceedings of the 1996 ASME Fluids Engineering Summer Meeting*, San Diego, 7–11 July, 1996, FED-238, p. 105.

[22] S. V. Patankar and D. B. Spalding, ''A calculation procedure for heat, mass and momentum transfer in three-dimensional parabolic flows,'' Int. J. Heat Mass Transfer **15**, 1787 (1972).

[23] R. J. A. Janssen, R. A. W. M. Henkes, and C. J. Hoogendoorn, ''Transition to time-periodicity of a natural convection flow in a 3D differentially heated cavity,'' Int. J. Heat Mass Transfer **36**, 2927 (1993).

[24] E. Hopf, ''Abzweigung einer periodischen Lösung von einer stationaren lösung eines differentialsystems,'' Ber. Verh. Sachs. Acad. Wiss. Leipzig Math. Nat. **94**, 3 (1942).

[25] B. D. Hassard, N. D. Kazarinoff, and Y. H. Wan, ''Theory and applications of Hopf bifurcation,'' London Math. Soc. Lecture Note Series **41**, 129 (1981).